

Near-real-time estimation of hourly open biomass burning emissions in China using multiple satellite retrievals

Yuanqian Xu ^{a,b}, Zhijiong Huang ^{a,b,*}, Jiamin Ou ^c, Guanglin Jia ^a, Lili Wu ^a, Huilin Liu ^a, Menghua Lu ^d, Meng Fan ^e, Jing Wei ^f, Liangfu Chen ^e, Junyu Zheng ^{a,b,*}

^a Institute for Environmental and Climate Research, Jinan University, Guangzhou 510632, China

^b Guangdong-Hongkong-Macau Joint Laboratory of Collaborative Innovation for Environmental Quality, Jinan University, Guangzhou 510632, China

^c Department of Sociology, Utrecht University, Padualaan 14, 3584, CH, Utrecht, Netherlands

^d College of Environment and Energy, South China University of Technology, Guangzhou 510641, China

^e State Key Laboratory of Remote Sensing Science, Aerospace Information Research Institute, Chinese Academy of Sciences, Beijing 100101, China

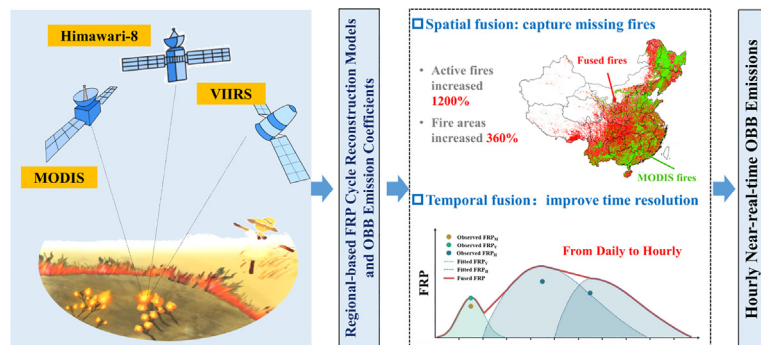
^f Department of Chemical and Biochemical Engineering, Iowa Technology Institute, University of Iowa, Iowa City, IA 52242, USA



HIGHLIGHTS

- A novel approach was developed to improve OBB emission estimations by fusing MODIS, VIIRS and Himawari-8 satellite observations.
- The novel approach can capture large part of fires missing by MODIS and promote the temporal resolution to an hour.
- The fusion of multiple satellites had increased the OBB emissions by about 5 times compared with previous estimates.
- The hourly peaks of OCB emissions were delayed by 1–4 h due to the escape from fire monitoring.

GRAPHICAL ABSTRACT



ARTICLE INFO

Article history:

Received 14 November 2021

Received in revised form 17 December 2021

Accepted 25 December 2021

Available online 4 January 2022

Editor: Jianmin Chen

Keywords:

Open biomass burning

Hourly estimation

Near-real-time emissions

Active fire fusions

ABSTRACT

Open biomass burning (OBB) is an important source of air pollutants and greenhouse gases, but its dynamic emission estimation remains challenging. Existing OBB emission datasets normally provide daily estimates based upon Moderate Resolution Imaging Spectroradiometer (MODIS) retrievals but tend to underestimate the emissions due to the coarse spatial resolution and sparse observation frequency. In this study, we proposed a novel approach to improve OBB emission estimations by fusing multiple active fires detected by MODIS, Visible Infrared Imaging Radiometer onboard the Suomi National Polar-orbiting Partnership (VIIRS S-NPP) and Himawari-8. The fusion of multiple active fires can capture the missing small fires and the large fires take place during the non-overpass time of MODIS observations. Also, regional-based fire radiative power (FRP) cycle reconstruction models and OBB emission coefficients were developed to address the large spatial discrepancies of OBB emission estimations across China and to promote the estimate to an hourly resolution. Using the new approach, hourly gridded OBB emissions in China were developed and can be updated with a lag of 1-day, or even near-real-time when real-time multiple active fires are available. OBB emissions in China based on this approach were more than 3 times of those in previous datasets. Evaluations revealed that the spatial distribution of the estimated PM_{2.5} emissions from this study was more consistent with the ambient PM_{2.5} concentrations during several episodes than existing datasets. The hourly OBB emissions provide new insight into its spatiotemporal variations, enhance timely and reliable air quality modeling and forecast, and support the formulation of accurate prevention and control policies of OBB.

* Corresponding authors at: Institute for Environmental and Climate Research, Jinan University, Guangzhou 510632, China.

E-mail addresses: bmmj@163.com (Z. Huang), zheng.junyu@gmail.com (J. Zheng).

1. Introduction

Open biomass burning (OBB) is an important source of air pollutants and greenhouse gases, posing a serious threat to air quality, climate change and human health (Tian et al., 2009; Jacobson, 2014; Chen et al., 2017; Akherati et al., 2020). It refers to the burning of crop residues, forest and other biomass in fields. Its emission fluctuates violently in line with the growing and harvest seasons in different regions. When its emissions peak at harvest seasons, its contribution to air quality can overweight important anthropogenic sources such as mobile sources and industry activities (Ding et al., 2013; Huang et al., 2014; Zhou et al., 2019; Yu et al., 2019; Cheng et al., 2021; Yadav et al., 2017; Bikkina et al., 2019; Paglione et al., 2020). For instance, it can contribute up to 37% to PM_{2.5} concentrations (Cheng et al., 2014), double the ozone formation potential of volatile organic compounds (VOCs) (Zhu et al., 2016) and contribute to 6.1% of the global mean effective radiative forcing driven by total anthropogenic in some regions of China during harvest seasons (Yao et al., 2017; IPCC, 2014).

Compared with other anthropogenic emission sources dominated by regular human activities, OBB is not only affected by human activities but is also largely affected by other less predictable factors like drought, lightning or other natural events (Xu et al., 2019; Wu et al., 2020). As a result, the spatiotemporal variations of OBB emissions stand out more than other anthropogenic emission sources. Conventionally, annual OBB emissions are calculated based on statistical and survey data (Streets et al., 2003; Li et al., 2016a; Li et al., 2016b; Azhar et al., 2019; Yang and Zhao, 2019; Singh et al., 2020). However, such OBB estimates generally lag 1 to 5 years behind due to the availability of activity data. Given the strong temporal variations of this source, such estimates are very likely outdated and cannot capture the spatial and temporal characteristics in the present. Advances in satellite observations provide alternative ways to achieve more up-to-date and dynamic OBB activity data. Several Moderate Resolution Imaging Spectroradiometer (MODIS) based global OBB emission datasets, such as Global Fire Emissions Database (GFED) (Van Der Werf et al., 2017), Fire INventory from NCAR (FINN) (Wiedinmyer et al., 2011), Global Fire Assimilation System (GFAS) (Kaiser et al., 2012), and Fire Energetics and Emissions Research (FEER) (Ichoku and Ellison, 2014), are available in daily basis. Nevertheless, they are still subject to some limitations. First, the spatial resolution of MODIS observations is not high enough (1 km for active fires and 500 m for burned area) and only limited detections (at 1:30, 10:30, 13:30 and 22:30 local time) are made per day. It results in 2 to 15 times underestimation of OBB emissions at a regional scale (Mao et al., 2014; Yang and Zhao, 2019; Pan et al., 2020). Second, the low frequency of MODIS overpass cannot be used to develop the hourly OBB emissions, contradictory to the fact that OBB has a strong temporal profile at hourly basis (Mota and Wooster, 2018; Li et al., 2019). Third, most global OBB emissions did not consider the regional discrepancies in developing or using the emission factors, which are varied by vegetation types and environmental conditions at regional scale (Schreier et al., 2015; Van Der Werf et al., 2017; Zhou et al., 2017).

To overcome the issues of underestimation and low temporal resolution, attempts have been made to combine MODIS monitoring and geostationary satellite observations for higher monitoring frequency. However, current studies mainly focused on large fires that occurred in the United States or Africa (Roberts et al., 2011; Li et al., 2019). For regions where most OBB generally contributes by open crop residue burning (OCB), these methods are not applicable since the size of active fires is too small to be detected by MODIS or geostationary satellites. Active fires, especially occurring at the non-overpass time of MODIS, are usually overlooked due to the coarse spatial resolution of geostationary satellites. The challenge to capture small active fires has not been addressed properly, hindering the accurate estimation of OBB emissions.

In this study, we posed a novel approach to dynamically estimate hourly OBB emissions by fusing multiple active fires from polar-orbiting and geostationary satellite observations. Besides MODIS observations (polar-orbiting), Visible Infrared Imaging Radiometer onboard the Suomi National Polar-orbiting Partnership (VIIRS S-NPP, polar-orbiting, 375 m, 2 times/

day, hereinafter referred to as VIIRS) detections and Himawari-8 monitoring (geostationary satellite, 2 km, observed every 10 min) are applied to improve the spatial coverage and temporal resolution in the OBB emission estimation. Also, regional fire radiative energy (FRE) based OBB emission coefficients are developed to reflect the regional discrepancies in the emission characteristics. This approach is used to develop a near-real-time hourly OBB emission inventory with only a 1-day lag and spatial resolution of 2 km in China. The emission products can help improve air quality modeling and forecast for pollution episodes in a timelier manner.

2. Data and methods

2.1. Methodological framework for the near-real-time estimation of OBB emissions

In this study, we proposed a novel approach by fusing multiple active fires from both polar-orbiting and geostationary satellites, and applied regional FRE-based emission coefficients to near-real-time estimate hourly OBB emissions (Fig. 1). In addition to the commonly used MODIS observations, VIIRS was applied to capture small fires that might be missed by MODIS (Li et al., 2018) and the Himawari-8 was applied to improve the temporal resolution of OBB emission estimates by constructing the hourly fire radiative power (FRP) variations of each gridded fire event (Bessho et al., 2016). To account for the large OBB emission discrepancies across the vast mainland caused by uneven climate conditions and vegetation types (Xu et al., 2019), OBB emissions in different regions and biomass types were estimated using different fusion parameters (FRP calibration factor, the burning duration (BD), FRP distributions, etc.) and FRE-based OBB emission coefficients. The approach consists of three major steps, including the collection and preprocessing of multiple active fires, spatial and temporal fusions, and regional FRE-based OBB emission estimation, which are presented in the following sections.

2.2. Data collection and preprocessing

Active fire products of MODIS and VIIRS used in this study were downloaded from the Fire Information for Resource Management System (FIRMS), NASA (<https://firms.modaps.eosdis.nasa.gov/>). Himawari-8 active fires were obtained from the P-Tree System, Japan Aerospace Exploration Agency (JAXA) (<https://www.eorc.jaxa.jp/ptree/>). These multiple active fires were preprocessed according to the following pretreatment procedures for accurate and easy fusion. First, active fires with low confidence ("<30%" for MODIS detections, "L" for VIIRS observations and "=1" for Himawari-8 monitoring) were deleted due to their large uncertainties on OBB detections (Randerson et al., 2012). Second, to account for the wide regional discrepancies of OBB emission estimations in China, the study area was divided into 7 OCB regions (Fig. 2a) according to the crop types (Mehmood et al., 2018; Qiu et al., 2016) and 4 forest regions (Fig. 2b) according to the spatial distribution of forest types. Thus, these active fires were assigned to 7 OCB regions and 4 forest regions based on land-use data and their locations. Third, active fires from MODIS, VIIRS and Himawari-8 in different regions were re-gridded and mapped to the same raster dataset with 2 km × 2 km horizontal resolutions and 1-hour intervals to facilitate temporal and spatial fusions (denoted as gridded active fires (GAF) and their FRP were denoted as FRP_M, FRP_V and FRP_H). We preferred to upscale multiple active fires to larger grid, rather than downscaling to finer grids. Because the precise location and FRP of finer pixels in MODIS or Himawari-8 observations are unknown, converting coarse active fires from MODIS or Himawari-8 observations to fine fires to match VIIRS will introduce significant uncertainty.

2.3. The fusion of multiple active fires

This section briefly introduces the methods for spatial and temporal fusions of multiple active fires, respectively. The details are available in Sections 2.3.1 and 2.3.2.

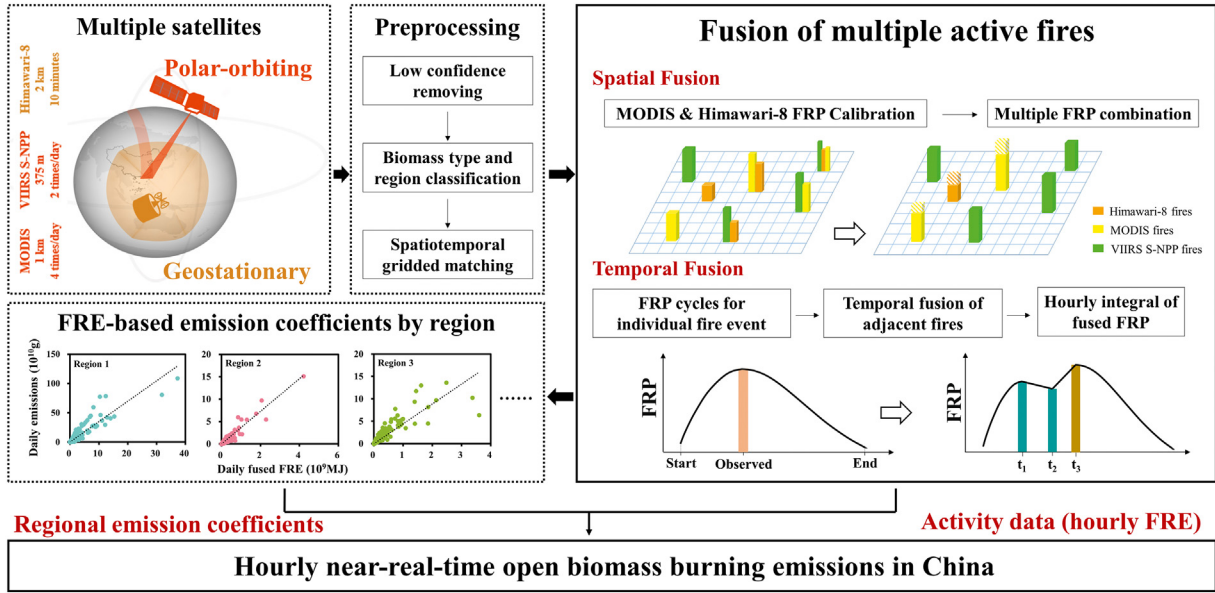


Fig. 1. The methodological framework for estimating the near-real-time OBB emissions.

2.3.1. Spatial fusion

The spatial fusion of active fires includes the FRP calibration and multiple FRP combination. First, the biased FRP_M and FRP_H caused by the coarse spatial resolution were calibrated based on the gridded FRP_V at different regions and biomass types. Due to its higher spatial resolution, VIIRS can detect small fires and thus typically observe more accurate and higher FRP values (Schroeder et al., 2014; Li et al., 2018). For instance, the cumulative contemporaneous FRP_M and FRP_H in China from July 2015 to June 2020 were 20% and 39% lower than the FRP_V , respectively. To get a better calibration, two methods were used to calibrate the FRP_M and FRP_H by region individually. 1) When contemporaneous $FRP_{V,t}$ and $FRP_{M,t}$ (or $FRP_{H,t}$) at the same grid were available, the entire FRP_H from the same fire event and the FRP_M were calibrated using Eqs. (1) and (2), respectively. To retain the shape of FRP_H distribution, the same adjustment factor $\frac{FRP_{V,t} - FRP_{H,t}}{FRP_{H,t}}$ derived from the hourly value was extended to the entire FRP_H . 2) To calibrate the remaining FRP_M or FRP_H , 11 averaged adjustment factors from different regions (7 OCB regions and 4 forest regions) were used. The calibration coefficients (α) of FRP_M and FRP_H were developed based on the identification of contemporaneous $FRP_{V,t}$ and $FRP_{M,t}$ (or $FRP_{V,t}$ and $FRP_{H,t}$) among 4.37

million OCB fires and 2.14 million forest fires from multiple satellite retrievals from July 2015 to June 2020. Ratios of the cumulative $FRP_{V,t}$ to $FRP_{M,t}$ and the cumulative $FRP_{V,t}$ to $FRP_{H,t}$ in different regions (see in Fig. S1) were used as α to calibrate FRP_M and FRP_H based on Eqs. (3) and (4). Second, the FRP_V and calibrated FRP_M and FRP_H were fused according to Eq. (5) to get a full dataset of FRP (FRP_f) and eliminate the repetitive FRP at the same grid and hour.

$$FRP_{sM} = FRP_M \times \frac{FRP_{V,t} - FRP_{M,t}}{FRP_{M,t}} \quad (1)$$

$$FRP_{sH} = FRP_H \times \frac{FRP_{V,t} - FRP_{H,t}}{FRP_{H,t}} \quad (2)$$

$$FRP_{sM} = \alpha \times FRP_M \quad (3)$$

$$FRP_{sH} = \alpha \times FRP_H \quad (4)$$

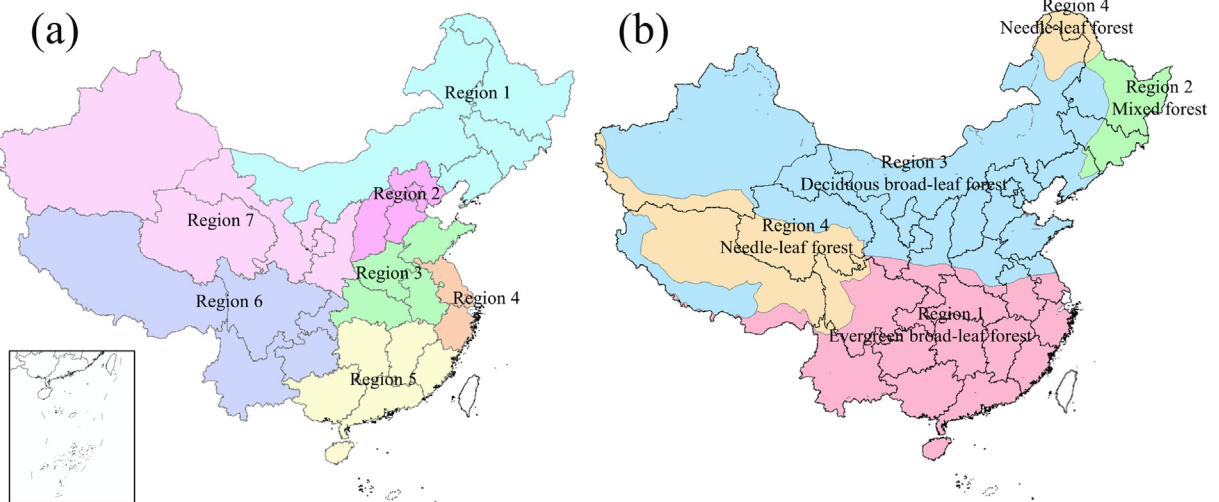


Fig. 2. Region divisions for OCB (a) and forest fires (b) in mainland China.

$$FRP_f = \begin{cases} FRP_V & \text{for } FRP_V > 0 \\ FRP_{sM} & \text{for } FRP_V = 0, FRP_M > 0 \\ FRP_{sH} & \text{for } FRP_V = 0, FRP_M = 0, FRP_H > 0 \end{cases} \quad (5)$$

where, FRP_{sM} and FRP_{sH} are the calibrated FRP_M , and FRP_H ; α is the ratios of cumulative $FRP_V, t / FRP_{M, t}$ and $FRP_V, t / FRP_{H, t}$.

2.3.2. Temporal fusion

The temporal fusion of multiple active fires includes the reconstruction of hourly FRP variations (denoted as FRP cycles) and the fusion of adjacent fires. The key of FRP cycle reconstruction was to estimate the BD and the FRP distribution using the prior information acquired from Himawari-8 continuous detections, which reveals that BD and distribution shapes are closely related to the peak FRP value of fire events. Therefore, a set of FRP cycle reconstruction models, including 11 regression models for estimating BD as a function of the peak FRP value and 86 FRP distributions as a function of BD in different regions were fitted using full FRP cycles obtained by Himawari-8.

To estimate BD for fire events, we identified all the single fire events according to the continuous observations of active fires from Himawari-8 from July 2015 to June 2020. These fire events were first assigned to 11 regions (7 OCB regions and 4 forest regions). The hourly FRP cycles of fire events with the same BD were averaged for different regions. Then, the regression models between BD and the peak FRP were developed for each region. Although most of the BD of fire events observed by Himawari-8 was larger than 4 h, those small fire events with the BD of less than 4 h can be predicted by the regression model. In this study, we set 2 h as the minimum BD of a fire event following the minimum BD of ~2 h observed by Vermote et al. (2009). BD for each region was calculated according to Eq. (6).

$$BD = \begin{cases} BD_{min} & \text{for } FRP < FRP_{min} \\ a \times FRP + b & \text{for } FRP_{min} \leq FRP \leq FRP_{max} \\ BD_{max} & \text{for } FRP > FRP_{max} \end{cases} \quad (6)$$

where, BD_{min} and BD_{max} represent the minimum and maximum values of the BD in a certain region, and BD_{min} is limited to 2 h for all regions. a and b are parameters for the liner relationship between BD and FRP. Parameters for the BD calculation were shown in Table S1.

Besides the BD, FRP distribution during a fire event were fitted according to the continuous detections of Himawari-8 FRP. For each region, fire events in different BD were clustered and their FRP cycles were averaged. A total of 86 distribution models (8 models for each region, excepted for OCB Region 4 and region5 with 7 models) were built based on Weibull distribution to portray these averaged hourly FRP cycles for fire events in different regions. The fitting FRP can be calculated based on Eq. (7).

$$FRP(t) = e^{(t_m/\lambda)^k} \cdot t_m^{(1-k)} \cdot FRP_{peak} \cdot t^{(k-1)} \cdot e^{-(t/\lambda)^k} \quad (7)$$

where, t_m and FRP_{peak} denote the time from the beginning and maximum FRP during a fire event. λ and k are scale and shape parameters for Weibull distribution and are presented in Table S2.

For fire events with BD larger than 4 h, FRP cycles were described by Weibull distribution fitted according to the continuous detections of Himawari-8 FRP. However, for those with BD less than 4 h, their FRP cycles were hardly fitted due to the lack of continuous monitoring. According to previous studies, the FRP cycles of most small fire events were Gaussian distributions (Vermote et al., 2009; Yang and Zhao, 2019; Liu et al., 2015). Therefore, in this study, we used Gaussian distributions to portray the FRP cycle (see Eq. (8)) for fire events with BD less than 4 h.

$$FRP(t) = FRP_{peak} * \left(e^{-\frac{(t-\mu)^2}{2\sigma^2}} \right) \quad (8)$$

where, μ and σ are parameters in Gaussian distributions. σ is assumed as a quarter of the BD, and μ is the middle time of the burning duration.

Because large fires can burn continuously for hours or even for a day, the adjacent active fires observed by multiple satellites may belong to the same fire event. In this study, to better characterize the hourly FRP variation, we fused the hourly FRP cycles of temporally adjacent active fires according to the difference between FFPR (predicted FRP of the former distribution at the X-value where the peak FRP of the latter distribution is located) and PFRP (the peak FRP of the latter distribution). Based on the observed FRP cycles of those long-burning events, we used the difference of 60% as the criterion to determine whether the adjacent active fires are from the same burning event. 1) If the difference between FFPR and PFRP is within $\pm 60\%$, these active fires are considered to be part of the same continuous burning process and then integrated to form a longer continuous FRP cycle to avoid the repeated integration of FRP from the same burning process (Fig. S2a). 2) If the difference between FFPR and PFRP is greater than 60%, these active fires are regarded as separate fire events and thus their FRP cycles were developed separately (Fig. S2b & c). Finally, the fused FRP was hourly integrated to gain hourly FRE according to Eq. (9).

$$FRE_{hh} = \int_{hh}^{hh+1} FRP(t) dt \quad (9)$$

where, hh means daily hour time from 0 to 23.

2.4. Development of regional FRE-based emission coefficients

FRE-based emission coefficients for OCB and forest fires were established individually to better reflect the considerable variations in OBB emission characteristics in different regions. Due to crop rotation, satellite data cannot adequately identify plant types for OCB, hence FRE-based OCB emission coefficients in different regions were developed based on historical emissions and the fused FRE from 2016 to 2019. To generate regional FRE-based OCB emission coefficients, 63 regression models for historical emissions and the fused FRE were built as follows. First, historical daily emissions from 2016 to 2019 in 7 OCB regions of China were developed using a combination of statistical data of crop products and the MODIS observations and active fire counts were applied to calibrate the in-field burning proportion (Xu et al., 2019). Second, regression models were developed to describe relationships between daily OCB emissions and fused FRE for 9 types of pollutants in each of the 7 OCB regions. Third, the slopes of the regression line between emissions and fused FRE were identified as the FRE-based OCB emission coefficients, as presented in Table 1.

Because forest vegetation types are relatively stable and can be accurately identified based on geographic information, regional FRE-based emission coefficients in different forest regions were developed by combining local dry matter-based emission factors and the biomass combustion coefficient (0.41 kg/MJ) (Xu et al., 2019; Vermote et al., 2009). FRE-based forest fire emission coefficients were also listed in Table 1.

Finally. The OBB emissions in China were calculated based on Eq. (10).

$$E_{i,j} = \sum_{g,hh,j} (FRE_{g,hh,j} \times EC_{i,j}) \quad (10)$$

Table 1
Regional FRE-based OBB emission coefficients (unit: g/MJ).

		CO	NOx	SO ₂	NH ₃	VOCs	PM _{2.5}	PM ₁₀	BC	OC
OCB	Region 1	34.80	2.15	0.35	0.47	5.22	6.53	7.26	0.18	1.94
	Region 2	36.30	2.27	0.46	0.35	5.13	6.33	6.46	0.19	2.35
	Region 3	42.69	2.42	0.49	0.47	4.96	6.82	7.64	0.24	2.67
	Region 4	39.52	1.85	0.27	0.60	3.75	5.91	7.84	0.22	1.87
	Region 5	44.32	1.83	0.14	0.84	3.94	6.63	9.73	0.23	1.55
	Region 6	30.42	1.93	0.34	0.37	4.67	5.72	6.14	0.15	1.79
	Region 7	31.07	1.91	0.38	0.31	4.28	5.35	5.56	0.16	1.98
Forest fires	Region 1	37.72	1.06	0.18	0.31	9.84	4.18	5.25	0.21	1.92
	Region 2	41.82	0.54	0.41	0.62	5.74	5.05	5.25	0.24	3.77
	Region 3	41.82	0.54	0.41	0.62	4.51	5.05	5.25	0.24	3.77
	Region 4	48.38	1.23	0.41	1.44	11.48	5.20	5.37	0.08	3.20

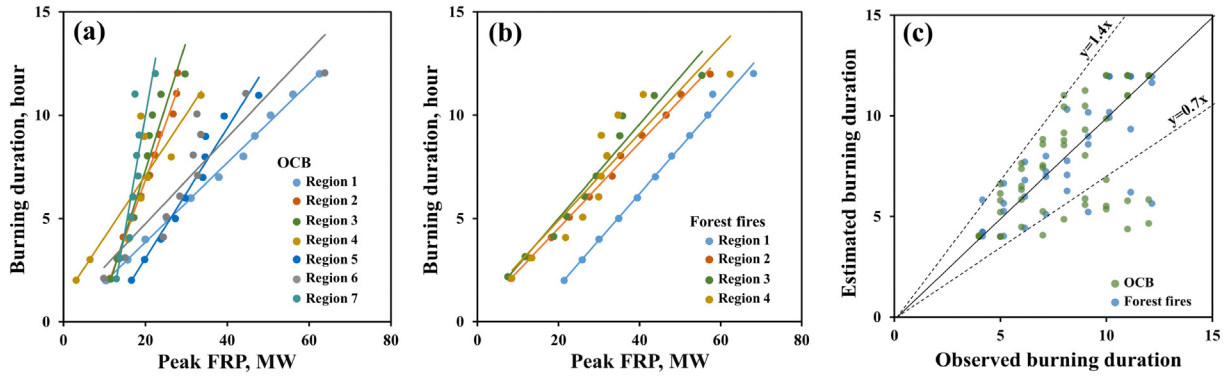


Fig. 3. Regression models between BD and peak FRP in the 7 OCB regions (a) and 4 forest regions (b). Comparisons of BD estimated in this study and observed by Himawari-8 (c).

where, g , i and j are the 2 km grid, pollutant and region. E_i means the OBB emissions for the i -th pollutant in China. $FRE_{g, hh, j}$ is the hh -th hourly FRE in the g -th grid and j -th region. $EC_{i,j}$ stands for the emission coefficients for the i -th pollutant in j -th region among the 7 OCB regions and 4 forest regions, which is presented in Table 1.

3. Results and discussion

3.1. Regional-based FRP cycle reconstruction models and OBB emission coefficients

An adequate prediction of BD is the key to reconstructing the FRP cycle of a fire event. In this study, we applied methods presented in Section 2.3.2 to build the models of the BD for 7 OCB regions and 4 forest regions. As revealed by 11 regression models in Fig. 3a & b, the linear relationship between the BD and peak FRP is evident across different regions, with the correlation coefficients (R) ranging from 0.71 to 0.99. This linear relationship is especially prominent when the peak FRP is approximately <30 MW in most models. Alternatively, when the peak FRP increases, the observed BD is more likely to deviate from the regression model. One reason is that larger fire events are more likely to involve several combustion stages. As revealed by the model parameters (see Table S1), the slopes of the regression models (a) range from 0.19 to 1.10. Among these models, the positive relationship between BD and peak FRP is consistent for forest fires, ranging from 0.20 to 0.23. Stable vegetation types and similar combustion

environment of forest fires are the main reasons for the moderate a in the 4 forest regions. In comparison, the linear relationships in OCB regions varied largely, possibly due to the regional discrepancies in crop types, planting habits and natural conditions. The maximum BD was identified as 12 h for most regions, except for OCB Region 4 and 5, which have a BD_{max} of 11 h. The regional differences among the above linear relationships reveal the need to develop regional-based models to capture the OBB emissions more reliably.

To validate the above regression models, the BD of fire events derived from Himawari-8 continuous observations from July 2020 to June 2021 were compared with the predicted BD (see Fig. 3c). It shows that the majority of BD of fire events can be well predicted by the regression models, with the correlation coefficients (R) of 0.62 and 0.73 for OCB and forest fires, respectively. Most of the paired BD (83%) were within the ratio of 0.7 to 1.4. The estimated-to-observed ratio of outliers is mainly less than 0.7, indicating that these fire events may be composed of several small fire events. For these fire events, we estimated BD for each small fire event and then fused them.

Another key to reconstructing the FRP cycle is to estimate the hourly FRP distribution of a fire event. According to the observations, the hourly FRP of fire events for all regions and combustion types increases sharply when an OBB event occurs and gradually decreases when it decays, showing a positive-skewed distribution. Weibull distribution is a good fit to describe the distribution characteristics. In this study, we developed 86 of Weibull distributions covering different BD in different regions, as shown in Fig. 4. All the parameters of 86 distributions were detailed in Table S2.

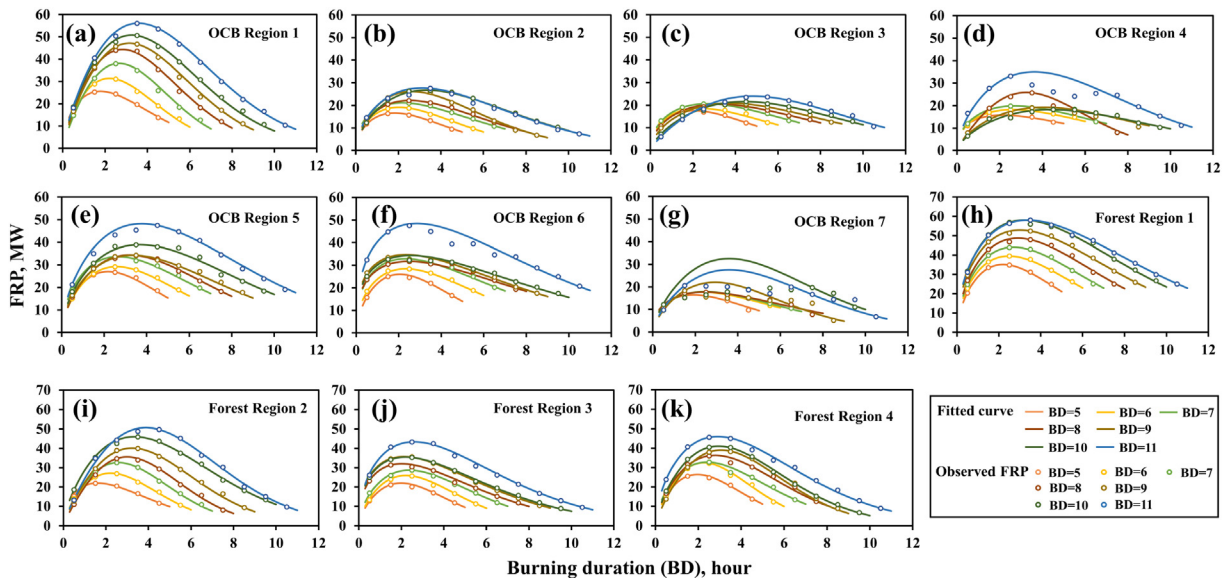


Fig. 4. Fitting models for the portraying of FRP distributions in OCB Region 1 to 7 (a-g), and Forest Region 1 to 4 (h-k).

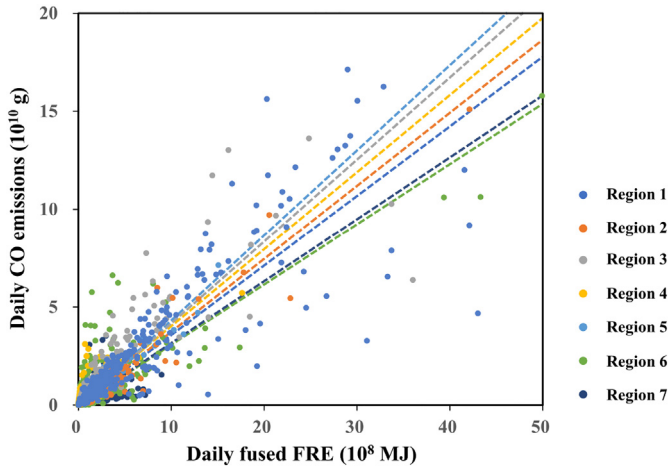


Fig. 5. Regression models between historical daily OCB emissions and fused FRE in different OCB regions.

As shown in these figures, the FRP distribution with the same BD showed large discrepancies across different regions, which are relevant to burn types and environmental conditions. Under the same BD, forest fires typically had a higher FRP than OCB since the burning size of forest fires is generally larger than OCB. This highlights the importance of developing regional FRP cycle reconstruction models. Moreover, when BD is 9 h or longer in parts of the regions (e.g., OCB Region 4 with BD = 11, OCB Region 6 with BD = 11 and OCB Region 7 with BD = 9, 10 and 11), the fitted FRP distribution tends to deviate from the observed values. These burnings with a long time and low FRP are probably composed of two or more small fire events, illustrating the necessity of temporal fusing for adjacent active fires.

Apart from the FRP cycle reconstruction models, the OCB emission coefficients also vary by region (Fig. 5). These emission coefficients were developed according to the correlation between historical daily emissions and fused FRE. The correlation, with the R ranging from 0.65 to 0.98, is highly linear positive across different regions in China, indicating that the OCB emissions were well estimated using region-based coefficients. The main causes for the discrepancies in emission coefficients lie in the differences in dry matter-based emission factors of different crop residues and cropping structures in different regions. For instance, the rice-dominated Region 5 tends to have the highest CO emission coefficients since the large dry matter-based emission factors of rice straw (64.2, 48.6 and 46.1 g/kg for

rice, wheat and corn straw) (Xu et al., 2019). These regional-based coefficients are comparable to the vast majority of those obtained through laboratory measurement or top-down constraining (Table S3).

3.2. Spatiotemporal improvements of fused active fires

In this section, we demonstrated how the spatial and temporal fusions improve the OBB estimation by filling in missing active fires and refining the temporal resolution. Fig. 6a & b shows the change in the spatial coverage of active fires as a result of the spatial fusion of MODIS, VIIRS and Himawari-8 from 2016 to 2020. In comparison to MODIS, VIIRS detected 1.49×10^5 extra GAF averaged per year, which is 5.9 times of the number of GAF detected by MODIS. Approximately 80% of these extra active fires were OCB and most of them were small fires. They were concentrated in Northeast China, where 21% of China's national grain production comes from (Yang et al., 2020). These extra small fires from VIIRS also result in an increase of 156% in the cumulative FRP. Besides the overlook of small fires, MODIS cannot capture a large portion of fires that occurred during its non-overpass time. This gap is partly filled by the Himawari-8, which can capture the fires by continuous monitoring. A large part of these additional fires are also captured in Northeast China with abundant crop residues and south China where forest fires take place. As a result, the spatial coverage of active fires has been improved by 2.96 times according to the Himawari-8 observations. By combining VIIRS and Himawari-8 with MODIS, the spatial coverage of active fires increased by 3.44 times. This means that previous OBB estimates based on single polar-orbiting satellite data, such as MODIS, might be significantly underestimated. The absence of active fires occurring during non-overpass time is the key cause of the underestimation, followed by the small fires.

We used the Sichuan Xichang forest fire as an example to illustrate how fusion improves temporal resolution. As shown in Fig. 6c, MODIS and VIIRS only provide 7 and 5 intermittent FRP observations, respectively, during the 69-h of forest fires (15:00 on 30 March ~12:00 on 2 April 2020). On the contrary, Himawari-8 provides more continuous FRP observations though there were still 20 h without FRP values due to the small size of these fires or the disturbance of the cloud (Wickramasinghe et al., 2018). In this study, these missing FRP values in the gap of Himawari-8 were interpolated using FRP distributions developed in Section 2.3.2 to form continuous hourly FRP. These estimated FRP values were then calibrated using the VIIRS observations to correct possible underestimations caused by the coarse resolution of Himawari-8. To assess the fused FRP, we compared the fused FRP-based and area-based biomass consumptions in four forest fire events (Fig. S3). The fused FRP-based biomass consumptions are

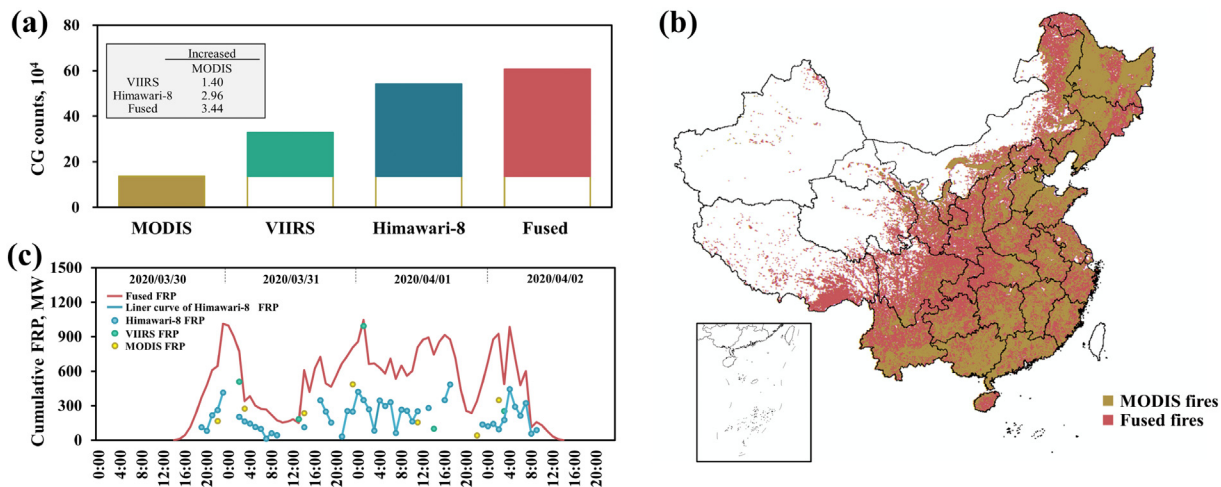


Fig. 6. The spatial coverage of active fires observed by MODIS and its increasing captured by VIIRS, Himawari-8 and fused active fires from 2016 to 2020 (a). Spatial distributions of MODIS and fused active fires from 2016 to 2020 (b). Hourly FRP variations from fused active fires, MODIS, VIIRS and Himawari-8 detections during the Sichuan Xichang forest fire from 30 March to 2 April 2020 (c).

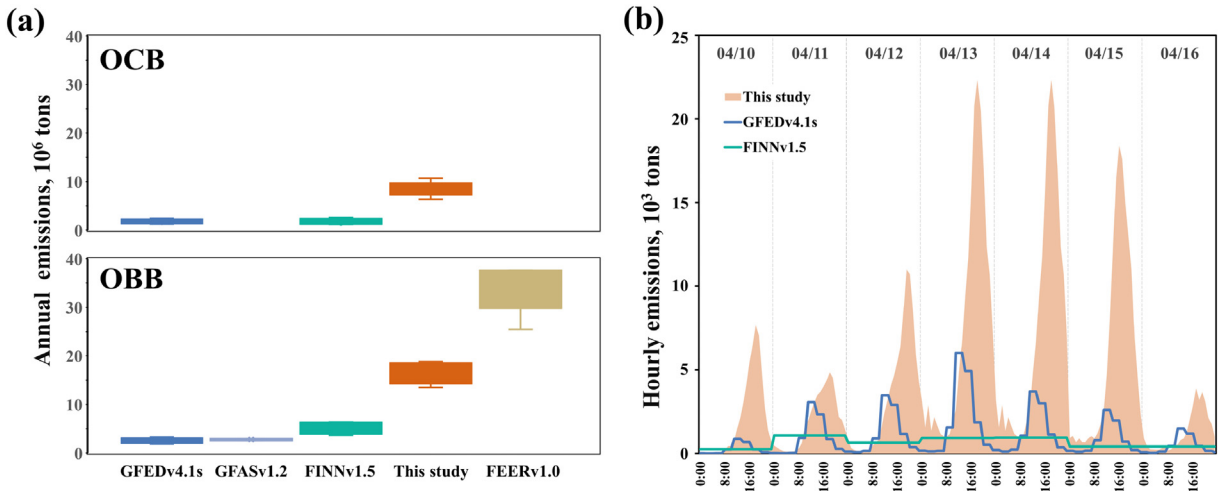


Fig. 7. Comparisons of annual mean CO emissions in this study and other MODIS-based OBB emission datasets (GFEDv4.1s, GFASv1.2, FINNv1.5 and FEERv1.0) from 2016 to 2020 (a). Hourly CO emissions estimated in this study, GFEDv4.1s and FINNv1.5 in Northeast China during an OCB event from April 10 to April 16, 2020 (b).

consistent with those estimates based on the burned area with slight underestimation, illustrating that the fused FRP could accurately capture the fire intensity.

3.3. Comparisons and evaluations

Based on the regional-based FRP cycle reconstruction models and emission coefficients, we created a dataset of hourly OBB emissions in China from 2016 to the present, with a spatial resolution of 2 km. So far, the dataset has been continuously updated on a daily basis. The fusion of multiple active fires increases the OBB emissions and partly resolves the underestimation of OBB emissions in previous datasets (Van Der Werf et al., 2017; Wiedinmyer et al., 2011; Kaiser et al., 2012; Ichoku and Ellison, 2014). To illustrate the emission change, annual CO emissions of OBB in China from 2016 to 2020 estimated in this study and other datasets, including GFEDv4.1s (Van Der Werf et al., 2017), FINNv1.5 (Wiedinmyer et al., 2011), GFASv1.2 (Kaiser et al., 2012) and FEERv1.0 (Ichoku and Ellison, 2014), were compared in Fig. 7a. Overall, mean annual CO emissions estimated in this study were 6.3, 5.9 and 3.3 times of those in the GFEDv4.1s, GFASv1.2 and FINNv1.5 datasets, respectively. Since these three global datasets only used MODIS retrievals, a large portion of active fires was excluded from the OBB emission estimation. The FEERv1.0 dataset was also developed using the MODIS FRP, but its estimates are about 2 times of our estimates. This is because the top-down FEERv1.0 emission coefficients developed by aerosol optical thickness were greatly overestimated in China (Ichoku and Ellison, 2014; Hammer et al., 2020). Another comparison also revealed that the FEERv1.0 emission coefficients in China were roughly 10 times larger than the regional FRE-based emission coefficients developed in this study (Table S3). Excluding the influence of the emission coefficients, the activity data adopted in this study was still about 5 times of that in the FEERv1.0.

In addition to the emission amount, the temporal and spatial characteristics of OBB emissions also improved. For demonstration, hourly CO emissions during an OCB event (from 10 April to 16 April 2020) in Northeast China were presented and compared to those estimates from GFEDv4.1s (3-h) and FINNv1.5 (daily) (Fig. 7b) (Van Der Werf et al., 2017; Wiedinmyer et al., 2011). The hourly OCB emissions estimated in this study have a higher temporal resolution. It revealed the large hourly variations in OCB emissions, which can be as high as two orders of magnitude. The diurnal patterns of OCB emissions, on the other hand, varied little from day to day with frequent peaks in the afternoon (around 17:00). In comparison, neither the GFEDv4.1s nor the FINNv1.5 captures the hourly variations. Although the GFEDv4.1s provides a diurnal cycle according to historical GOES observations during 2007–2009 in the western hemisphere

(Van Der Werf et al., 2017), the diurnal cycle was assumed to be periodical in all days, resulting in the underestimation of some emission peaks.

By filling a large part of missing fires, OBB emissions estimated in this study were more spatially consistent with observations than those estimates solely using MODIS. For instance, the PM_{2.5} emissions estimated in this study (fused-based emissions) were more widely distributed and consistent with the ambient PM_{2.5} concentrations derived from satellite observations (Wei et al., 2020; Wei et al., 2021) than those estimated solely based on MODIS retrievals (MODIS-based emissions) (Fig. 8). The correlation (R) between the fused-based emissions and observed PM_{2.5} concentrations increased from 0.31 to 0.62, compared to MODIS-based emissions. Also, a similar improvement in spatial consistency between emissions and observed PM_{2.5} concentrations was observed during another OBB emission episode in October 2017 (Fig. S4).

In this study, we also used uncertainty analysis to assess the OBB emission estimates retrieved from multiple active fires. Sources of uncertainties in OBB emission estimates include FRP observations, BD and FRP distribution models, and emission coefficients. According to Freeborn et al. (2014), the coefficient of variation (CV) of MODIS FRP for an individual fire pixel was 53%, and it decreased to ~5% after upscaling. Because active fires with low confidence were removed during the preprocessing, the CV of observed FRP was assumed to be 5%. Based on the comparison of the estimated BD and FRP with observations, uncertainties of estimated BD and FRP were quantified as ± 40% and ± 10%, respectively. Following previous studies, the CV of CO, NOx, SO₂, NH₃, VOCs, PM_{2.5}, PM₁₀, BC and OC emission coefficients were quantified as 58%, 55%, 79%, 67%, 97%, 65%, 50%, 66% and 70%, respectively (Andreae, 2019). Then, we used the Monte Carlo simulation to propagate uncertainties in BD, FRP and emission coefficients to emission estimates. Results show that uncertainties of OBB emissions in China were -64% to 94%, -63% to 93%, -78% to 114%, -70% to 106%, -93% to 137%, -68% to 101%, -59% to 87%, -68% to 103% and -71% to 104% for CO, NOx, SO₂, NH₃, VOCs, PM_{2.5}, PM₁₀, BC and OC emissions in 2020 (95% confidence intervals). Compared with OBB emissions from previous studies (Yang and Zhao, 2019; Li et al., 2016b) based on MODIS observations (uncertainties ranges from -83% ~ -52% to 126% ~ 303%), uncertainties in this study decreased, indicating that the fusion of multiple active fires can reduce uncertainties in OBB emissions.

3.4. Variations of OBB emissions in China

Based on the dataset of hourly OBB emissions developed in this study, the spatiotemporal variations of OBB emissions in China from 2016 to 2020 were analyzed. In this section, we used CO emissions as an example

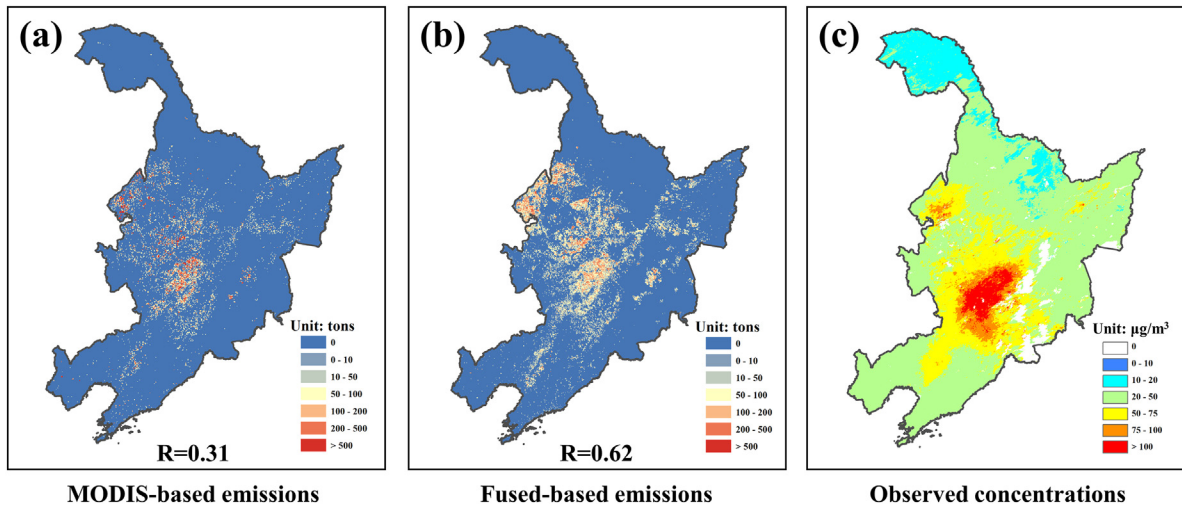


Fig. 8. Spatial distributions of MODIS-based PM_{2.5} emissions (a), fused-based OBB PM_{2.5} emissions (b) and MODIS-observed PM_{2.5} concentrations (c) (Wei et al., 2020; Wei et al., 2021) in April 2020 in Northeast China.

to examine the spatiotemporal variation. In terms of the annual emission trend, OBB emissions in China have decreased in recent years, falling from 1.81×10^7 tons in 2016 to 1.52×10^7 tons in 2020, owing to the prohibition on crop residue burning and the prevention of forest fires (Fig. 9a & b). However, OCB emissions in Northeast China (OCB Region 1) continued to rise 28% with fluctuations, indicating that there is still large room for reduction. As shown in Fig. 10, Northeast China is the hot spot of OBB emissions in China, which contributed 24% and 44% of the total OBB and OCB

emissions in 2020, respectively. Possible explanations for the high OCB emission in Northeast China were its high grain production and the incomplete coverage of the supervise period (details see in the exploration of peak hour changes).

At daily and hourly scales, the dataset reveals a large temporal variation in OBB emissions, especially at the hourly scale. In China, 95% of the daily national OBB emissions varied between 23% and 434% of the daily average, and 95% of the hourly national OBB emissions varied between 10%

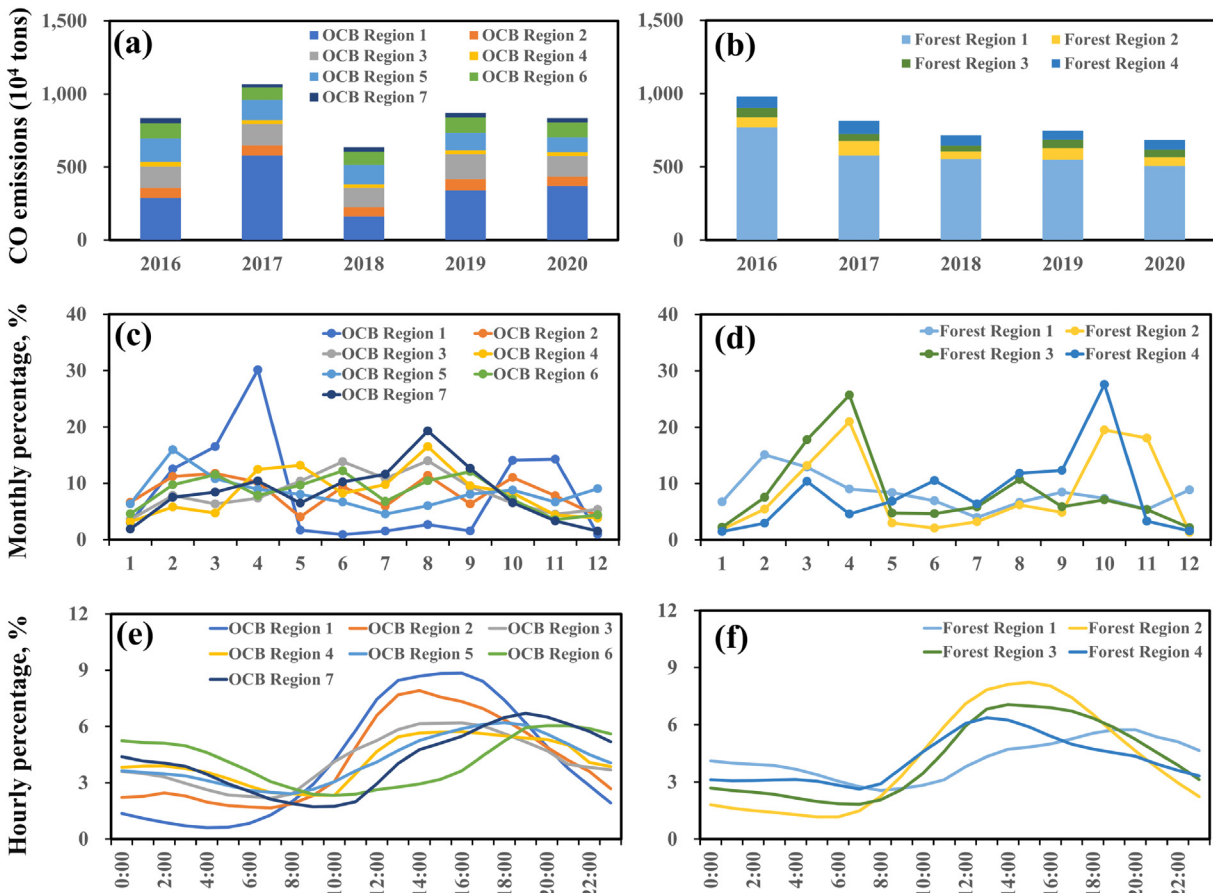


Fig. 9. Annual CO emissions from OCB (a) and forest fires (b), monthly patterns of OCB emissions (c) and forest fire emissions (d), hourly patterns of OCB emissions (e) and forest fire emissions (f) in different regions.

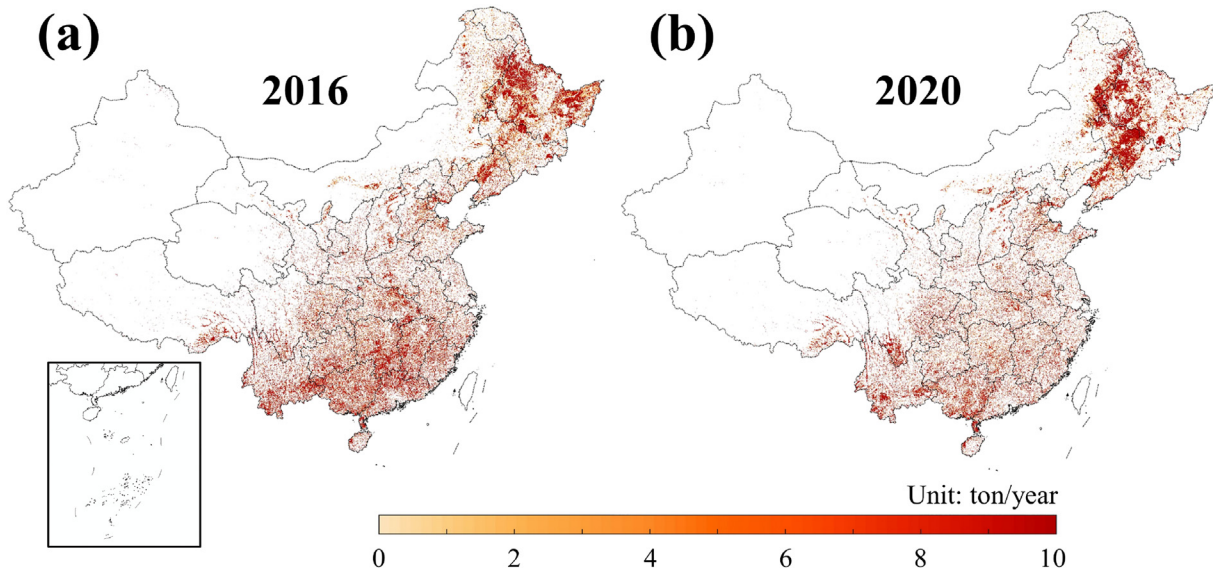


Fig. 10. Spatial distributions of CO emissions from OBB in 2016 (a) and 2020 (b) in China.

and 632% of the hourly average. Moreover, these temporal variations in OBB emissions vary dramatically across regions. Fig. 9c & d reveal a significant discrepancy in monthly patterns in various regions, especially for OCB emissions. The main reason for regional differences in monthly patterns is crop planting habits. In OCB Region 1, for example, crops are primarily planted in March and April and harvested in October, resulting in 47% and 28% of OCB emissions concentrated in March to April and October to November, respectively. In addition, we presented the average hourly changes of OBB emissions for different regions in China (Fig. 9e & f). Overall, both hourly OCB and forest fire emissions vary significantly throughout the day, with peaks in the afternoon and troughs around 08:00, similar to the diurnal FRP across the conterminous United States (Li et al., 2019). Because of the geographical difference in vegetation types, natural conditions, human activities and control policies, hourly variations of OBB emissions also differed remarkably by region. These differences in temporal variations and diurnal variations highlight the importance of estimating hourly OBB emissions by region.

Based on the temporal resolution of the dataset, we also find a gradual change in hourly variations and emissions peaks. The four regions with the largest OCB emissions (OCB Region 1, 3, 5 and 6) were selected to

demonstrate the annual change of peak hours of OCB emissions. As shown in Fig. 11, the peak hour of OCB emissions in these regions had been pushed backward by 1–4 h in recent years. Hourly emissions from 10:00 to 15:00 had decreased, particularly at 13:00 and 14:00, with an average reduction of about 17%, while hourly emissions from 18:00 to 21:00 increased by 28%. The backward shift of the emission peak is more obvious in OCB Region 1, where OCB emissions at 13:00 decreased by about 20% while OCB emissions at 17:00 increased by about 42%. The strict control measures of OBB may be the main cause of the backward shift. Since 1999, China has implemented several control measures to regulate OBB emissions, which were gradually tightened in 2008, 2013 and 2015. Specific control measures include strengthening the supervision of open burning, increasing crop straw utilization, and so on. Fire observations from MODIS were widely used to monitor biomass burning and to evaluate the control measures. However, it may not be completely effective because MODIS only passes over four times per day. Moreover, some regions (especially in OCB Region 1) can postpone biomass burning events by several hours to escape the monitoring, resulting in shifts of OBB emission peaks, from 13:00 to 17:00. The approach established in this study can provide hourly OBB emissions and support for 24-hour supervision.

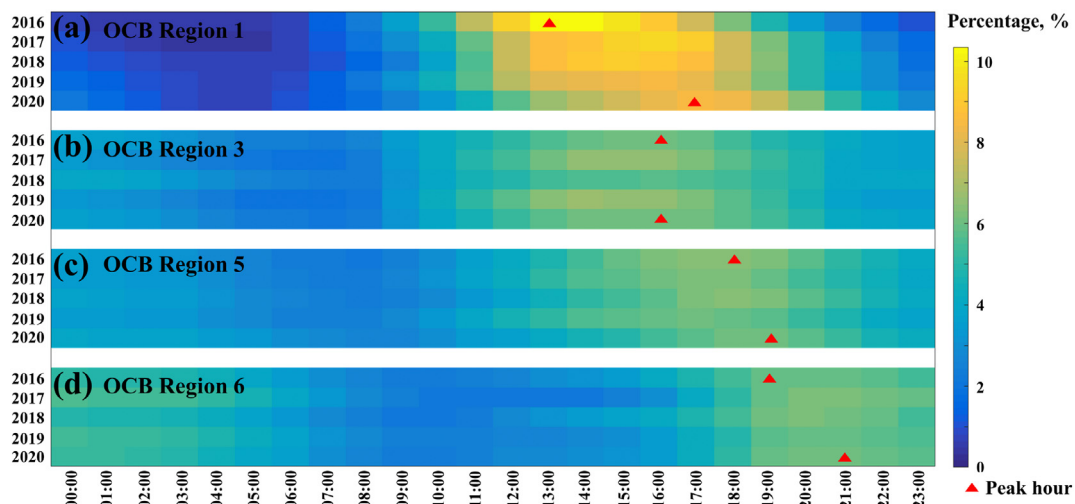


Fig. 11. Hourly patterns of OCB emissions from 2016 to 2020 in typical regions (a. OCB Region 1; b. OCB Region 3; c. OCB Region 5; d. OCB Region 6).

4. Conclusions and implications

In this study, we proposed a novel approach for estimating hourly OBB emissions. The approach addressed the underestimation issue and low temporal resolution of previous OBB estimates by fusing multiple active fires from polar-orbiting and geostationary satellite observations. In comparison to previous OBB estimates solely based on MODIS observations (Van Der Werf et al., 2017; Wiedinmyer et al., 2011; Kaiser et al., 2012; Ichoku and Ellison, 2014), the novel approach can capture some small fires that MODIS may have missed, as well as some relatively large fires that occur outside the overpass time of MODIS, and thus can provide a more accurate description of the spatial characterization and coverage of OBB emissions with only a 1-day lag. In the case study of China, these small fires and active fires during non-overpass time contributed 25% and 53% of the total spatial coverage of fused active fires, respectively. As a result, 95% of national OBB emissions were concentrated in 14% of the Chinese territory, higher than the 5% captured only by MODIS retrievals.

Furthermore, the novel approach can promote the temporal resolution of OBB emission estimations from 1 day to 1 h, which is significantly higher than most previous daily OBB emission estimates, as well as the timeliness. Relying on a set of regional-based FRP cycle reconstruction models derived from Himawari-8 observations, it is also possible to provide near-real-time OBB emissions when the multiple active fires come in timely. These advancements enable us to capture the temporal variability, dynamic changes and latest status of OBB emissions, which could help to identify new regulatory actions for timely and precise control of OBB emissions. For instance, we found a very significant temporal variation in OBB emissions and the backward shift of hourly peaks of OCB emissions in several regions in China.

Aside from emission estimates, the novel approach can be used to improve air quality modeling and forecasting. Previous studies reported that biomass burning is an important source of ambient PM_{2.5}, accounting for about 10% of PM_{2.5} formations in China on average (Zhu et al., 2018). However, most model-ready OBB emissions with a temporal resolution of 1 h were developed based on prescribed temporal profiles and the annual estimate. As a result, the temporal variations of OBB emissions in the model were largely underestimated, which in turn led to a large bias in simulating pollution formation associated with OBB emissions. By using the novel approach, the right temporal and spatial variations of OBB emissions can be input into the model and forecasting system. Moreover, by identifying and quantifying the OBB spatiotemporal variations and their driving forces based on the historical hourly emissions, it is promising to predict short-time OBB emissions to further improve forecasting.

Although the novel approach improves OBB estimates, it has several limitations. First, small fires that occurred at the non-overpass time of VIIRS or MODIS are still ignored. Due to the coarse spatial resolution, these small fires cannot be detected by Himawari-8 monitoring. This means that the OBB emissions developed in this study are still partly underestimated. To further address the underestimation of small fires, more satellite retrievals, such as VIIRS on board the National Oceanic and Atmospheric Administration-20 (NOAA-20), the Advanced Geosynchronous Radiation Imager (AGRI) onboard the Feng Yun-4A (FY4A), should be fused. Second, rather than field study, the regional OBB emission coefficients employed in this study are generated using data investigation and regression models. Although these emission coefficients are comparable with most of the existing studies, large uncertainties still exist in the OBB emission characterization. To better quantify OBB emissions, localized OBB emission coefficients for different regions should be carried out in line with the extensive field study.

CRediT authorship contribution statement

Yuanqian Xu: Conceptualization, Writing – original draft, Methodology, Validation, Formal analysis. **Zhijiong Huang:** Methodology, Validation, Writing – review & editing. **Jiamin Ou:** Writing – review & editing. **Guanglin Jia:** Data curation, Visualization. **Lili Wu:** Data curation. **Huilin**

Liu: Visualization. **Menghua Lu:** Visualization. **Meng Fan:** Resources. **Jing Wei:** Resources. **Liangfu Chen:** Resources. **Junyu Zheng:** Conceptualization, Methodology, Writing – review & editing, Supervision.

Declaration of competing interest

The authors declare that they have no known competing financial interests or personal relationships that could have appeared to influence the work reported in this paper.

Acknowledgements

We are grateful for the financial support of the National Key R&D Program of China (No. 2018YFC0213904), the Key-Area Research and Development Program of Guangdong Province (No. 2019B110206001) and the National Natural Science Foundation of China (No. 41805068). We acknowledge the use of MODIS and VIIRS S-NPP active fire products provided by NASA/Fire Information for Resource Management System (FIRMS), and the Himawari-8 active fires product supplied by the P-Tree System, Japan Aerospace Exploration Agency (JAXA).

Appendix A. Supplementary data

Supplementary data to this article can be found online at <https://doi.org/10.1016/j.scitotenv.2021.152777>.

References

- Akherati, A., He, Y., Coggon, M., Koss, A., Hodshire, A., Sekimoto, K., Warneke, C., Gouw, J., Yee, L., Seinfeld, J., Onasch, T., Herndon, S., Knighton, W., Cappa, C., Kleeman, M., Lim, C., Kroll, J., Pierce, J., Jathar, S., 2020. Oxygenated aromatic compounds are important precursors of secondary organic aerosol in biomass-burning emissions. *Environ. Sci. Technol.* 54, 8568–8579.
- Andreae, M., 2019. Emission of trace gases and aerosols from biomass burning—an updated assessment. *Atmos. Chem. Phys.* 19, 8523–8546.
- Azhar, R., Zeeshan, M., Fatima, K., 2019. Crop residue open field burning in Pakistan, multi-year high spatial resolution emission inventory for 2000–2014. *Atmos. Environ.* 208, 20–33.
- Bessho, K., Date, K., Hayashi, M., Ikeda, A., Imai, T., Inoue, H., Kumagai, Y., Miyakawa, T., Murata, H., Ohno, T., Okuyama, A., Oyama, R., Sasaki, Y., Shimazu, Y., Shimoji, K., Sumida, Y., Suzuki, M., Taniguchi, H., Tsuchiya, H., Uesawa, D., Yokota, H., Yoshida, R., 2016. An introduction to Himawari-8/9—Japan's new-generation geostationary meteorological satellites. *J. Meteorol. Soc. Japan.* 94, 151–183.
- Bikkina, S., Andersson, A., Kirillova, E., Holmstrand, H., Tiwari, S., Srivastava, A., Bisht, D., Gustafsson, Ö., 2019. Air quality in megacity Delhi affected by countryside biomass burning. *Nat. Sustain.* 2, 200–205.
- Chen, J., Li, C., Ristovski, Z., Milic, A., Gu, Y., Ialam, M., Wang, S., Hao, J., Zhang, H., He, C., Guo, H., Fu, H., Miljevic, B., Morawska, L., Thai, P., LAM, Y., Pereira, G., Ding, A., Huang, X., Dumka, U., 2017. A review of biomass burning: Emissions and impacts on air quality, health and climate in China. *Sci. Total Environ.* 579, 1000–1034.
- Cheng, Z., Wang, S., Fu, X., Watson, J., Jiang, J., Fu, Q., Chen, C., Xu, B., Yu, J., Chow, J., Hao, J., 2014. Impact of biomass burning on haze pollution in the Yangtze River delta, China: a case study in summer 2011. *Atmos. Chem. Phys.* 14, 4573–4585.
- Cheng, Y., Yu, Q., Liu, J., Du, Z., Liang, L., Geng, G., Zheng, B., Ma, W., Qi, H., Zhang, Q., He, K., 2021. Strong biomass burning contribution to ambient aerosol during heating season in a megacity in Northeast China: effectiveness of agricultural fire bans? *Sci. Total Environ.* 754, 142144.
- Ding, A., Fu, C., Yang, X., Sun, J., Zheng, L., Xie, Y., Herrmann, E., Nie, W., Petäjä, T., Kerminen, V., Kulmala, M., 2013. Ozone and fine particle in the western Yangtze River Delta: an overview of 1 yr data at the SORPES station. *Atmos. Chem. Phys.* 13, 5813–5830.
- Freeborn, P.H., Wooster, M.J., Roy, D.P., Cochrane, M.A., 2014. Quantification of MODIS fire radiative power (FRP) measurement uncertainty for use in satellite-based active fire characterization and biomass burning estimation. *Geophys. Res. Lett.* 41 (6), 1988–1994.
- Hammer, M., van Donkelaar, A., Li, C., Lyapustin, A., Sayer, A., Hsu, N., Levy, R., Garay, M., Kalashnikova, O., Kahn, R., Brauer, M., Apte, J., Henze, D., Zhang, L., Zhang, Q., Ford, B., Pierce, J., Martin, R., 2020. Global estimates and long-term trends of fine particulate matter concentrations (1998–2018). *Environ. Sci. Technol.* 54, 7879–7890.
- Huang, R., Zhang, Y., Bozzetti, C., Ho, K., Cao, J., Han, Y., Daellenbach, K., Slowik, J., Platt, S., Canonaco, F., Zotter, P., Wolf, R., Pieber, S., Bruns, E., Crippa, M., Ciarelli, G., Piazzalunga, A., Schwikowski, M., Abbaszade, G., Schnelle-Kreis, J., Zimmermann, R., An, A., Szidat, S., Baltensperger, U., Haddad, I.E., Prévôt, A., 2014. High secondary aerosol contribution to particulate pollution during haze events in China. *Nature* 514, 218–222.
- Ichoku, C., Ellison, L., 2014. Global top-down smoke-aerosol emissions estimation using satellite fire radiative power measurements. *Atmos. Chem. Phys.* 14, 6643–6667.

- IPCC, 2014. Anthropogenic and natural radiative forcing. Climate Change 2013 – The Physical Science Basis: Working Group I Contribution to the Fifth Assessment Report of the Intergovernmental Panel on Climate Change. Cambridge University Press, Cambridge, pp. 659–740 659 – 740.
- Jacobson, M.Z., 2014. Effects of biomass burning on climate, accounting for heat and moisture fluxes, black and brown carbon, and cloud absorption effects. *J. Geophys. Res.-Atmos.* 119, 8980–9002.
- Kaiser, J., Heil, A., Andreae, M., Benedetti, A., Chubarova, N., Jones, L., Morcrette, J., Razinger, M., Schultz, M., Suttie, M., Van Der Werf, G., 2012. Biomass burning emissions estimated with a global fire assimilation system based on observed fire radiative power. *Biogeosciences* 9, 527–554.
- Li, J., Li, Y., Bo, Y., Xie, S., 2016a. High-resolution historical emission inventories of crop residue burning in fields in China for the period 1990–2013. *Atmos. Environ.* 138, 152–161.
- Li, J., Bo, Y., Xie, S., 2016b. Estimating emissions from crop residue open burning in China based on statistics and MODIS fire products. *J. Environ. Sci.* 44, 158–170.
- Li, F., Zhang, X., Kondragunta, S., Csiszar, I., 2018. Comparison of fire radiative power estimates from VIIRS and MODIS observations. *J. Geophys. Res.-Atmos.* 123, 4545–4563.
- Li, F., Zhang, X., Roy, D., Kondragunta, S., 2019. Estimation of biomass-burning emissions by fusing the fire radiative power retrievals from polar-orbiting and geostationary satellites across the conterminous United States. *Atmos. Environ.* 211, 274–287.
- Liu, M., Song, Y., Yao, H., Kang, Y., Li, M., Huang, X., Hu, M., 2015. Estimating emissions from agricultural fires in the North China plain based on MODIS fire radiative power. *Atmos. Environ.* 112, 326–334.
- Mao, Y.H., Li, Q.B., Chen, D., Zhang, L., Hao, W.M., Liou, K.N., 2014. Top-down estimates of biomass burning emissions of black carbon in the Western United States. *Atmos. Chem. Phys.* 14, 7195–7211.
- Mehmood, K., Chang, S., Yu, S., Wang, L., Li, P., Li, Z., Liu, W., Rosenfeld, D., Seinfeld, J., 2018. Spatial and temporal distributions of air pollutant emissions from open crop straw and biomass burnings in China from 2002 to 2016. *Environ. Chem. Lett.* 16, 301–309.
- Mota, B., Wooster, M.J., 2018. A new top-down approach for directly estimating biomass burning emissions and fuel consumption rates and totals from geostationary satellite fire radiative power (FRP). *Remote Sens. Environ.* 206, 45–62.
- Paglione, M., Gilardoni, S., Rinaldi, M., Decesari, S., Zanca, N., Sandrini, S., Giulianelli, L., Bacco, D., Ferrari, S., Poluzzi, V., Scotto, F., Trentini, A., Poulaïn, L., Herrmann, H., Wiedenhofer, A., Canonaco, F., Prevot, A., Massoli, P., Carbone, C., Facchini, M., Fuzzi, S., 2020. The impact of biomass burning and aqueous-phase processing on air quality: a multi-year source apportionment study in the Po Valley. Italy. *Atmos. Chem. Phys.* 20, 1233–1254.
- Pan, X., Ichoku, C., Chin, M., Bian, H., Darmenov, A., Colarco, P., Ellison, L., Kucsera, T., Silva, A., Wang, J., Oda, T., Cui, G., 2020. Six global biomass burning emission datasets: inter-comparison and application in one global aerosol model. *Atmos. Chem. Phys.* 20, 969–994.
- Qiu, X., Duan, L., Chai, F., Wang, S., Yu, Q., Wang, S., 2016. Deriving high-resolution emission inventory of open biomass burning in China based on satellite observations. *Environ. Sci. Technol.* 50, 11779–11786.
- Randerson, J., Chen, Y., Van Der Werf, G., Rogers, B., Morton, D., 2012. Global burned area and biomass burning emissions from small fires. *J. Geophys. Res.-Biogeosci.* 117, G04012.
- Roberts, G., Wooster, M., Freeborn, P., Xu, W., 2011. Integration of geostationary FRP and polar-orbiter burned area datasets for an enhanced biomass burning inventory. *Remote Sens. Environ.* 115, 2047–2061.
- Schreier, S., Richter, A., Schepaschenko, D., Shvidenko, A., Hilboll, A., Burrows, J., 2015. Differences in satellite-derived NO_x emission factors between eurasian and north american boreal forest fires. *Atmos. Environ.* 121, 55–65.
- Schroeder, W., Oliva, P., Giglio, L., Csiszar, I., 2014. The new VIIRS 375 m active fire detection data product: algorithm description and initial assessment. *Remote Sens. Environ.* 143, 85–96.
- Singh, T., Biswal, A., Mor, S., Ravindra, K., Singh, V., Mor, S., 2020. A high-resolution emission inventory of air pollutants from primary crop residue burning over northern India based on VIIRS thermal anomalies. *Environ. Pollut.* 266, 115132.
- Streets, D., Yarber, K., Woo, J., Carmichael, G., 2003. Biomass burning in Asia: annual and seasonal estimates and atmospheric emissions. *Global Biogeochem. Cy.* 17, 1099.
- Tian, D., Hu, Y., Wang, Y., Boylan, J., Zheng, M., Russell, A., 2009. Assessment of biomass burning emissions and their impacts on urban and regional PM2.5: a Georgia case study. *Environ. Sci. Technol.* 43, 299–305.
- Van Der Werf, G., Randerson, J., Giglio, L., Van Leeuwen, T., Chen, Y., Rogers, B., Mu, M., Van Marle, M., Morton, D., Collatz, G., Yokelson, R., Kasibhatla, P., 2017. Global fire emissions estimates during 1997–2016. *Earth. Syst. Sci. Data.* 9, 697–720.
- Vermote, E., Ellicott, E., Dubovik, O., Lapayonok, T., Chin, M., Giglio, L., Roberts, G., 2009. An approach to estimate global biomass burning emissions of organic and black carbon from MODIS fire radiative power. *J. Geophys. Res.-Atmosph.* 114, D18.
- Wei, J., Li, Z., Cribb, M., Huang, W., Xue, W., Sun, L., Guo, J., Peng, Y., Li, J., Lyapustin, A., Liu, L., Wu, H., Song, Y., 2020. Improved 1 km resolution PM2.5 estimates across China using enhanced space-time extremely randomized trees. *Atmos. Chem. Phys.* 20, 3273–3289.
- Wei, J., Li, Z., Lyapustin, A., Sun, L., Peng, Y., Xue, W., Su, T., Cribb, M., 2021. Reconstructing 1-km-resolution high-quality PM2.5 data records from 2000 to 2018 in China: spatiotemporal variations and policy implications. *Remote Sens. Environ.* 252, 112136.
- Wickramasinghe, C., Wallace, L., Reinke, K., Jones, S., 2018. Intercomparison of Himawari-8 AHI-FSA with MODIS and VIIRS active fire products. *Int. J. Digit. Earth.* 13, 457–473.
- Wiedinmyer, C., Akagi, S., Yokelson, R., Emmons, L., Al-Saadi, J., Orlando, J., Soja, A., 2011. The fire INventory from NCAR (FINN): a high resolution global model to estimate the emissions from open burning. *Geosci. Model Dev.* 4, 625–641.
- Wu, J., Kong, S., Wu, F., Cheng, Y., Zheng, S., Qin, S., Liu, X., Yan, Q., Zheng, H., Zheng, M., Yan, Y., Liu, D., Ding, S., Zhao, D., Shen, G., Zhao, T., Qi, S., 2020. The moving of high emission for biomass burning in China: view from multi-year emission estimation and human-driven forces. *Environ. Int.* 142, 105812.
- Xu, Y., Huang, Z., Jia, G., Fan, M., Cheng, L., Chen, L., Shao, M., Zheng, J., 2019. Regional discrepancies in spatiotemporal variations and driving forces of open crop residue burning emissions in China. *Sci. Total Environ.* 671, 536–547.
- Yadav, I., Devi, N., Li, J., Syed, J., Zhang, G., Watanabe, H., 2017. Biomass burning in Indo-China peninsula and its impacts on regional air quality and global climate change—a review. *Environ. Pollut.* 227, 414–427.
- Yang, Y., Zhao, Y., 2019. Quantification and evaluation of atmospheric pollutant emissions from open biomass burning with multiple methods: a case study for the Yangtze River Delta regionChina. *Atmos. Chem. Phys.* 19, 327–348.
- Yang, G., Zhao, H., Tong, D.Q., Xiu, A., Zhang, X., Gao, C., 2020. Impacts of post-harvest open biomass burning and burning ban policy on severe haze in the northeastern China. *Sci. Total Environ.* 716, 136517.
- Yao, H., Song, Y., Liu, M., Archer-Nicholls, S., Lowe, D., McFiggans, G., Xu, T., Du, P., Li, J., Wu, Y., Hu, M., Zhao, C., Zhu, T., 2017. Direct radiative effect of carbonaceous aerosols from crop residue burning during the summer harvest season in East China. *Atmos. Chem. Phys.* 17, 5205–5219.
- Yu, M., Yuan, X., He, Q., Yu, Y., Cao, K., Yang, Y., Zhang, W., 2019. Temporal-spatial analysis of crop residue burning in China and its impact on aerosol pollution. *Environ. Pollut.* 245, 616–626.
- Zhou, Y., Xing, X., Lang, J., Chen, D., Cheng, S., Wei, L., Wei, X., Liu, C., 2017. A comprehensive biomass burning emission inventory with high spatial and temporal resolution in China. *Atmos. Chem. Phys.* 17, 2839–2864.
- Zhou, Y., Luo, B., Li, J., Hao, Y., Yang, W., Shi, F., Chen, Y., Simayi, M., Xie, S., 2019. Characteristics of six criteria air pollutants before, during, and after a severe air pollution episode caused by biomass burning in the southern Sichuan BasinChina. *Atmos. Environ.* 215, 116840.
- Zhu, Y., Yang, L., Chen, J., Wang, X., Xue, L., Sui, X., Wen, L., Xu, C., Yao, L., Zhang, J., Shao, M., Lu, S., Wang, W., 2016. Characteristics of ambient volatile organic compounds and the influence of biomass burning at a rural site in northern China during summer 2013. *Atmos. Environ.* 124, 156–165.
- Zhu, Y., Huang, L., Li, J., Ying, Q., Zhang, H., Liu, X., Hong, L., Li, N., Liu, Z., Mao, Y., Fang, H., Hu, J., 2018. Sources of particulate matter in China: insights from source apportionment studies published in 1987–2017. *Environ. Int.* 115, 343–357.